Supplementary Information

Title: FeNi Intermetallic Compound Nanoparticles Wrapped by N-doped Graphitized Carbon: A novel Cocatalyst for Boosting PC Hydrogen Evolution

Sibo Chen,[a] Xunfu Zhou,[a] Jihai Liao,[b] Siyuan Yang,[a] Xiaosong Zhou,[c] Qiongzhi Gao,[a] Shanqing Zhang,*[d] Yueping Fang,*[a, e] Xinhua Zhong [a, e] and Shengsen Zhang*[a, e]

[a] College of Materials and Energy, South China Agricultural University, Guangzhou, 510642, PR China.

*E-mail: zhangss@scau.edu.cn; ypfang@scau.edu.cn

[b] Department of Physics, South China University of Technology, Guangzhou 510640, P. R. China.

[c] School of Chemistry and Chemical Engineering, Institute of Physical Chemistry, Lingnan Normal University, Zhanjiang, 524048, China.

[d] Centre for Clean Environment and Energy and School of Environment and Science, Griffith University, Gold Coast, QLD 4222, Australia.

*E-mail: s.zhang@griffith.edu.au

[e] Guangdong Laboratory for Lingnan Modern Agriculture, Guangzhou, 510643, China

Contents

Part I: Density functional theory calculations

Part II: Experimental Section

Part III: Supplementary Results

Part IV: References

Part I: Density functional theory calculations

Our calculations were performed based on the density functional theory (DFT) applied in the Vienna Ab initio Simulation Package (VASP). [1] Projector augmented wave (PAW) potentials [2] with Spin-polarized generalized gradient approximation (GGA) in Perdew-Burke-Ernzerhof (PBE) [3] format was used for the exchange-correlation potential. The plane-wave cutoff energy was set at 450 eV. Ni(111) and FeNi(111) surfaces were modeled by a four-layer periodic slab with a vacuum thickness of 15 Å. The upper two layers and the adsorbates were allowed to relax until all residual forces declined below 0.01 eV/Å, while the bottom two layers were fixed. The reciprocal space is represented by the Monkhorst-Pack special k point scheme [4] with a density of grid points along with x and y directions about $2\pi \times 0.02 \text{ Å}^{-1}$.

The adsorption energies (E_{ads}) of a H_2 atom on substrates were calculated as follows.

$$E_{ads} = E_0 - \frac{1}{2}E_{H_2} - E_s$$

Where E_0 and E_s represent the total energies per cell with and without adsorbed H atom and E_{H_2} indicates the total energy of an H_2 molecule. [5,6]

Part II: Experimental Section

2.1 Chemical reagents

Potassium ferricyanide ($K_3[Fe(CN)_6]$), sodium citrate ($C_6H_5Na_3O_7$), nickel nitrate hexahydrate ($Ni(NO_3)_2 \cdot 6H_2O$), and ferric ferrocyanide ($Fe_4[Fe(CN)_6]_3$) were sourced from Aladdin. TiO_2 was purchased from Degussa and urea (AR) was bought from Damao. All the involved chemical reagents were used as purchased and not further purified.

2.2 Synthesis process

Preparation of Ni₃[Fe(CN)₆]₂·H₂O nanocubes and FeNi@NGC nanoparticles.

$Ni_3[Fe(CN)_6]_2 \cdot H_2O$ nanocubes were prepared in line with the method described in the literature.[7] In a typical synthesis, a 200 ml solution of $Ni(NO_3)_2 \cdot 6H_2O$ (6 mmol) and sodium citrate (9 mmol) was mixed with 200 ml $K_3Fe(CN)_6$ (4 mmol) solution. The mixed solution was agitated for 5 min then aged for 24 h. Then, the resulting precipitates were separated by centrifugation, washed and dried in vacuum at 60 ℃ (Figure S1, Supporting Information). The FeNi@NGC nanoparticles were fabricated by the pyrolysis of $Ni_3[Fe(CN)_6]_2 \cdot H_2O$, which is described in Figure S1c by thermogravimetric analysis (TGA). In a typical process, after grinding, 1.0 g $Ni_3[Fe(CN)_6]_2 \cdot H_2O$ powder was transferred into a porcelain boat and annealed in N_2 at 650 ℃ for 2 h. The resulting black solid powder was FeNi@NGC nanoparticles.

Preparation of Fe@NGC and Ni@NGC nanoparticles. In the case of N_2 as a protective gas, 1 g of $Fe_4[Fe(CN)_6]_3$ was calcined at 900 ℃ for 2 h to obtain Fe@NGC nanoparticles. 0.2 g of $Ni(NO_3)_2 \cdot 6H_2O$ and 1 g of g-C_3N_4 were stirred and dried in

ethanol solution before being calcined at 800 ℃ for 2 h to derive Ni@NGC nanoparticles.

Preparation of g-C₃N₄. Typically, 20 g of urea was placed in a porcelain crucible with a cover and then calcined at 600 °C for 2 h in a muffle furnace with a heating rate of 5 °C min^{-1}. The pristine g-C$_3$N$_4$ was obtained after cooling to room temperature.

Preparation of FeNi@NGC/g-C₃N₄, Fe@NGC/g-C₃N₄, and Ni@NGC/g-C₃N₄. By mechanically grinding a mixture of g-C$_3$N$_4$ and FeNi@NGC with varying FeNi@NGC content at mass ratios of 5%, 10%, 15%, and 20%. After grinding for 1 h, the obtained samples were labeled as FNC5, FNC10, FNC15, and FNC20, respectively. The Fe@NGC/g-C$_3$N$_4$ and Ni@NGC/g-C$_3$N$_4$ photocatalysts were obtained using an identical method.

Preparation of hollow carbon spheres-modified g-C₃N₄. The FeNi@NGC nanoparticles were dispersed in HCl solution (1M) and then stirred for 6 h. After centrifugal drying, the hollow carbon spheres (HCS) were derived (Figure S3a, Supporting Information). Subsequently, the same mechanical grinding method was used for the preparation of HCS/g-C$_3$N$_4$.

Preparation of FeNi@NGC/TiO₂. Typically, 0.08 g of FeNi@NGC nanoparticles and 2 g of TiO$_2$ were added into 40 ml ethanol and dried by stirring at 60 °C. The photocatalysts obtained by calcining at 300 °C for 2 h under N$_2$ were recorded as 4%-FN/TiO$_2$. The 2%-FN/TiO$_2$ and 6%-FN/TiO$_2$ samples were obtained in the same way.

Preparation of 1.0%Pt/g-C₃N₄ and 1.0%Pt/TiO₂ photocatalyst. 1.0 wt.% Pt was loaded on the surface of g-C$_3$N$_4$ and TiO$_2$ photocatalysts by in situ photo-deposition method

using H_2PtCl_6 to prepare the 1.0%Pt/g-C_3N_4 and 1.0%Pt/TiO_2 photocatalyst, respectively. [8]

Preparation of N-doped carbon (NC) coated FeCo IMC (FeCo@NC), Fe@NC and Ni@NC. 1.0 g of $Na_2CoFe(CN)_6$ nanocubes were placed in porcelain boat and calcined at 500 ℃ for 4 h under N_2 protection with a heating rate of 5 °C min^{-1}, and a black solid powder, i.e., FeCo@NC nanoparticles, was obtained. $Co(NO_3)_2 \cdot 6H_2O$ and g-C_3N_4 were added into anhydrous ethanol and stirred evenly, then dried at 60 ℃ and calcined at 800 ℃ for 2 h to obtain Co@NC nanoparticles. Similarly, Fe@NC nanoparticles were obtained from $FeCl_3$ and g-C_3N_4 as raw materials calcining at 900 ℃ for 2 h. Preparation of FeCo@NC/g-C_3N_4 composite photocatalyst was done by mechanical grinding of g-C_3N_4 and FeCo nanoparticles in agate mortar.

Preparation of FeCo@NC/g-C_3N_4, Fe@NC/g-C_3N_4 and Co@NC/g-C_3N_4. Preparation of the FeCo@NC/g-C_3N_4 composite photocatalyst was done by mechanical grinding of g-C_3N_4 (90%) and FeCo nanoparticles (10%) for 1h in agate mortar. The Co@NC/g-C_3N_4 and Fe@NC/g-C_3N_4 composite photocatalysts were produced in the same way.

2.3 Characterization

The X-ray diffraction (XRD) spectra were recorded using Rigaku D/MAX 2500 v/PC at 5 ℃ min^{-1}. The morphology and distribution of material were examined by using field emission scanning electron microscope (FESEM) and transmission electron microscope (TEM), both of which were purchased from Philips FEI Quanta. X-ray photoelectron spectroscopy (XPS) records were obtained with ESCALB 250

equipment. N_2 adsorption and desorption curve as well as pore size distribution information were obtained by Mc ASAP2460. The photoluminescence (PL) spectra were obtained on a Perkin-Elmer LS-50 B fluorescence spectrometer (Perkin Elmer, Inc., USA) with an excitation wavelength of 379 nm and the PL decay plots were detected using an Edinburgh Instruments F980 at room temperature. The mass ratios of Fe and Ni in FeNi@NGC were detected by inductively coupled plasma atomic emission spectroscopy (ICP-AES) analysis using a PerkinElmer Plasma 400 spectrophotometer. EIS was examined at a 5 mV of alternating current signal in the frequency range of 0.01e106 Hz on a PGSTAT30 Eco Chemie B. V. electrochemical workstation.

2.4 Photoelectrochemical measurements

10 mg of photocatalysts and 10 μl 0.5% Nafion solution were added into 5 ml ethanol before dispersion by ultrasound. The solution of 500 μl was deposited on FTO conductive glass (2 cm × 3 cm) 10 times in total. The FTO glass deposited with photocatalyst was calcined at 150 °C for 1 hour by using nitrogen as the protective gas, after which the working electrode was prepared. The calcined FTO glass, the platinum plate, and the Ag/AgCl (saturated KCl) were taken as the working, the counter, and the reference electrodes, respectively, to form a three-electrode system. Mott-Schottky, electrocatalytic H_2 evolution, electrochemical impedance spectroscopy, and transient photocurrent were measured at an electrochemical workstation (Zahner-Elektrik IM6E35). Linear sweep voltammetry (LSV) at a 5 mV s^{-1} scan rate was performed by an electrochemical analyzer with a three-electrode

system in an electrolyte solution of 0.5 M Na_2SO_4. Rotating disk electrode (RDE) or rotating ring-disk electrode (RRDE) testing was performed using a Pine Modulated Speed rotator with the GC disk diameter of 5 mm and the Pt ring width of 1 mm. LSV were carried out on RDE or RRDE (15.5 uL catalyst ink, catalyst loading 0.261 mg cm^{-2}) in the oxygen saturated 0.1 M KOH solution from 0.0 V to 1.0 V (vs. RHE) with rotation speeds of 1600 rpm at a scan rate of 10 mV s^{-1}.

2.5 Photocatalytic (PC) H_2 evolution measurements

In a traditional PC H_2 evolution experiment, 20 mg of the photocatalysts was dispersed in 15% triethanolamine aqueous solution (15ml/100 ml) and 100 ml solution was transferred to a sealed quartz magnetic top irradiation reactor. A 300 W Xenon lamp was taken as the light source, and the visible light was obtained by an optical filter to cut off the light in the ultraviolet region in the g-C_3N_4-based photocatalyst systems. The TiO_2-based photocatalyst process for H_2 evolution uses ultraviolet-visible light as the light source. N_2 bubbles in the reactor for over 30 min to create an anaerobic environment in the reactor before illumination. After the reaction started, 400 µl gas was extracted from the reactor every hour and analyzed using gas chromatography (GC-7900) to calculate the efficiency of the PC H_2 evolution. PC H_2 generation for overall pure water splitting was carried out in a LabSolar 6A PC H_2 evolution system (Perfectlight, Beijing) under white light (300 W Xe arc lamp) irradiation.

2.6 Calculation of apparent quantum yield

In a typical formula for calculating the apparent quantum yield (AQY) of photocatalyst, the lights of different wavelength range were obtained by using the Xenon lamp as

the light source with different optical filter. The light intensity was measured by UV spectrum analyzer (OHSP-350UV, Hangzhou HOPOO, wavelength range within 340–780 nm). R_{H_2} (µmol/h) represents H_2 evolution rate, E (W/cm^2) represents monochromatic light intensity, A (cm^2) represents the light radiation area of the reaction system, λ (m) represents monochromatic wavelength, t_1 (h), t_2 (s), h (W) and c (m/s) substituted into 1, 3600, 6.626 $\times$ 10^{-34} and 3 $\times$ 10^8, respectively [9].

$$AQY\ (\%) = \frac{number\ of\ reached\ electrons}{number\ of\ incident\ photons} \times 100$$

$$= \frac{number\ of\ evolved\ H_2\ molecules\ \times 2}{number\ of\ incident\ photons} \times 100$$

$$= \frac{2R_{H_2}t_1N_A}{EAt_2\lambda/hc} = 6.6482 \times 10^{-5} \times R_{H_2}/(E \times A \times \lambda)$$

Part III: Supplementary Results
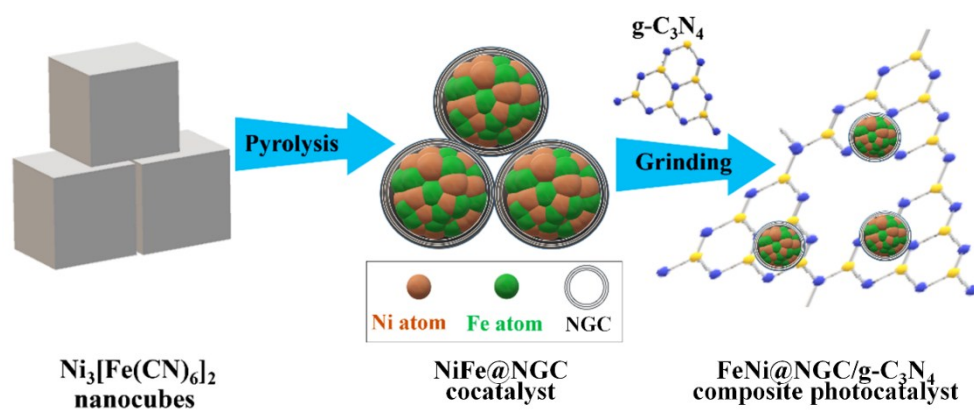
Scheme S1. Schematic illustration of the syntheses of FeNi@NGC cocatalyst and FeNi@NGC/g-C$_3$N$_4$ composite photocatalyst for the application of highly enhanced PC H$_2$ generation.

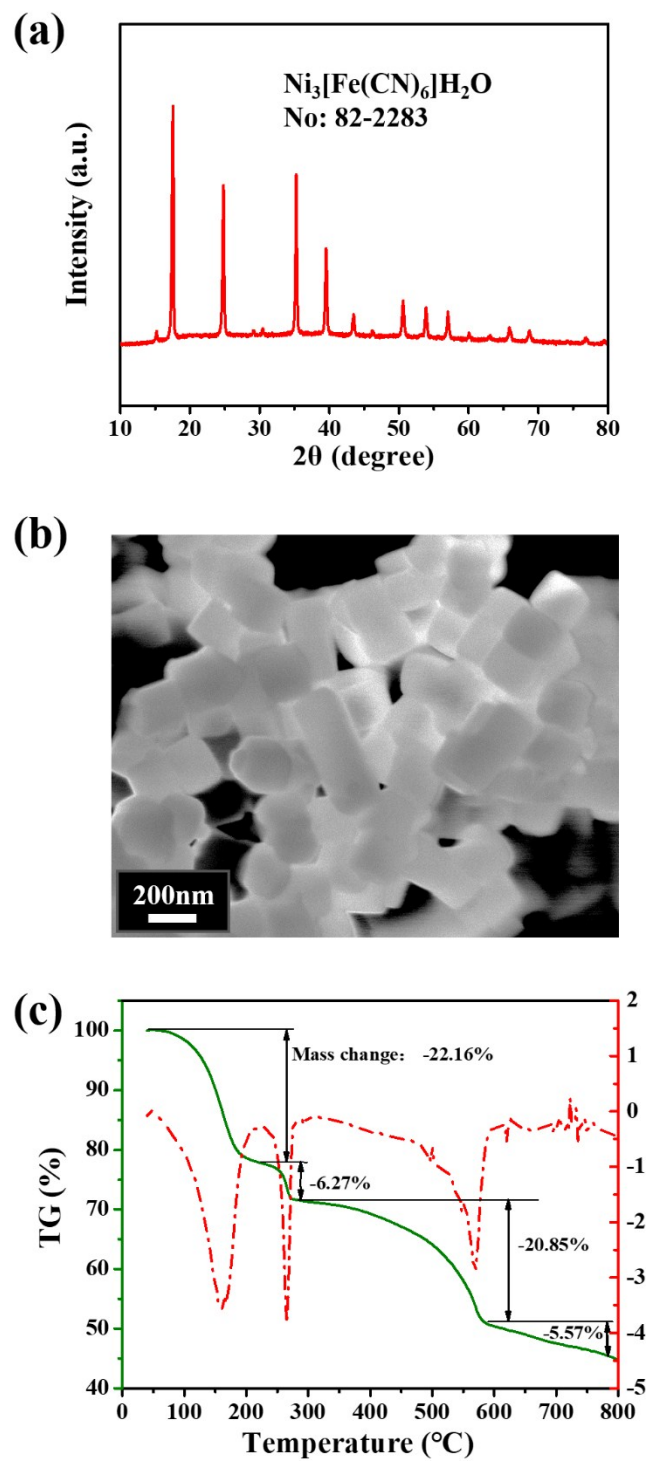**Figure S1.** XRD pattern (a), SEM image (b) and TG analysis (c) for $Ni_3(Fe(CN)_6)_2$.

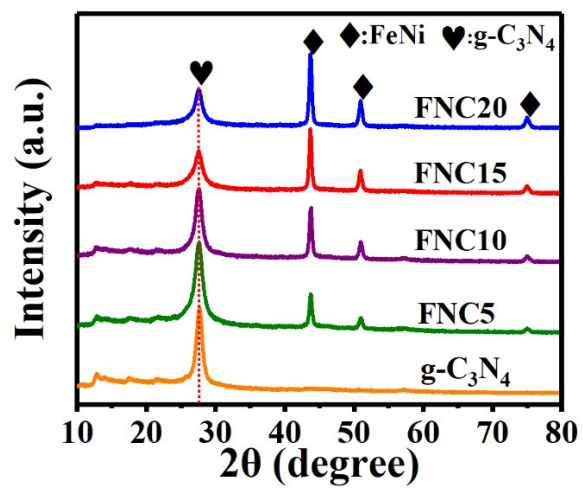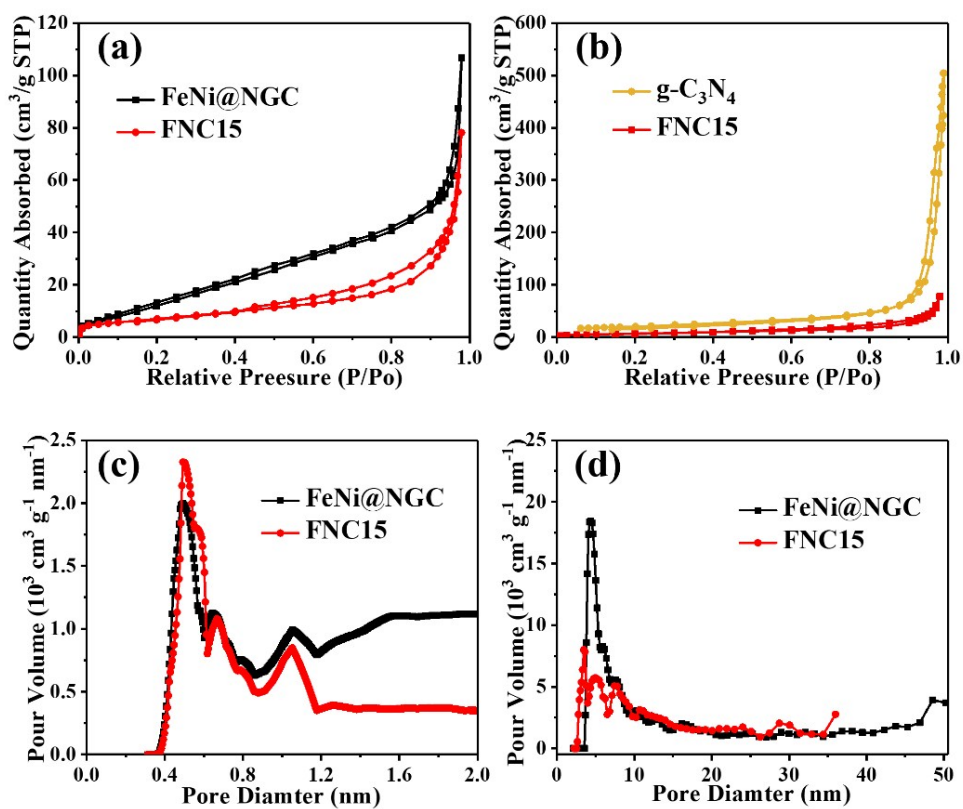**Figure S2.** XRD patterns of g-C$_3$N$_4$ and FNC samples.

Figure S3. Adsorption-desorption curve of FeNi@NGC and FNC15 (a), g-C_3N_4 and FNC15 (b). Pore size distribution of FeNi@NGC and FNC15 (c, d).
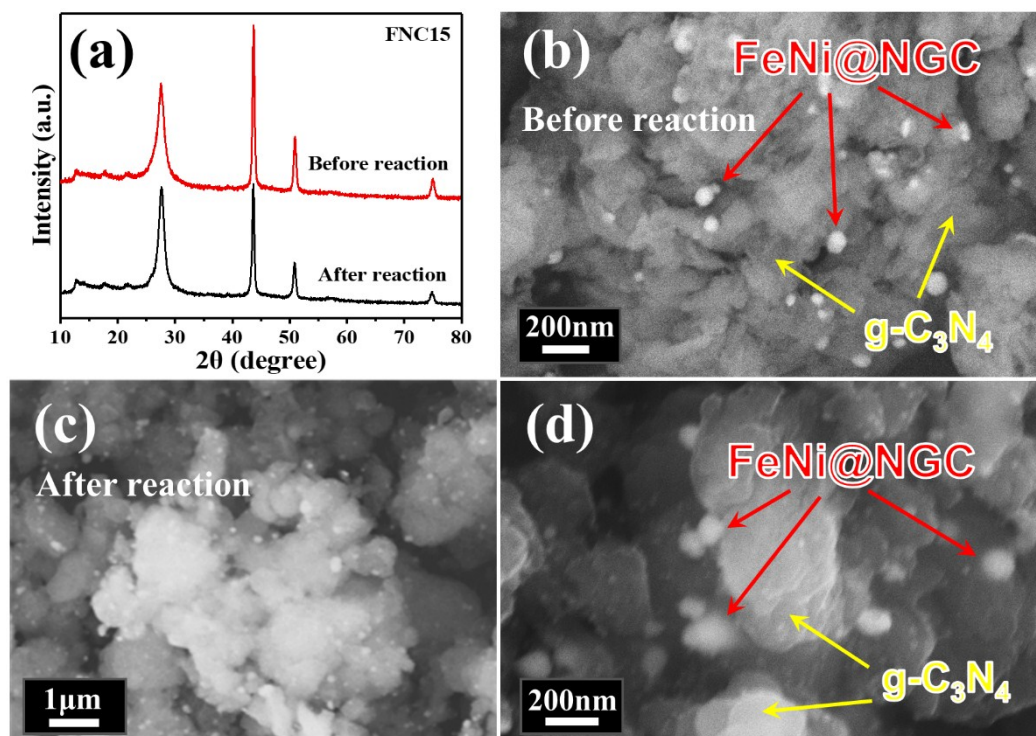
Figure S4. (a) XRD pattern of FNC15 before and after reaction, SEM of FNC15 before

reaction (b) and after reaction (c and d).

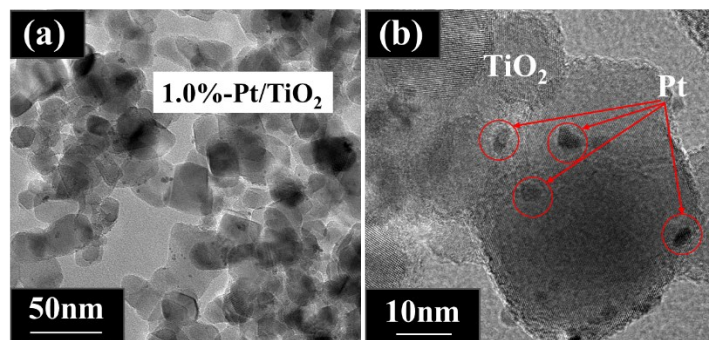**Figure S5.** TEM (a) and HRTEM (b) images of 1.0%-Pt/TiO$_2$.
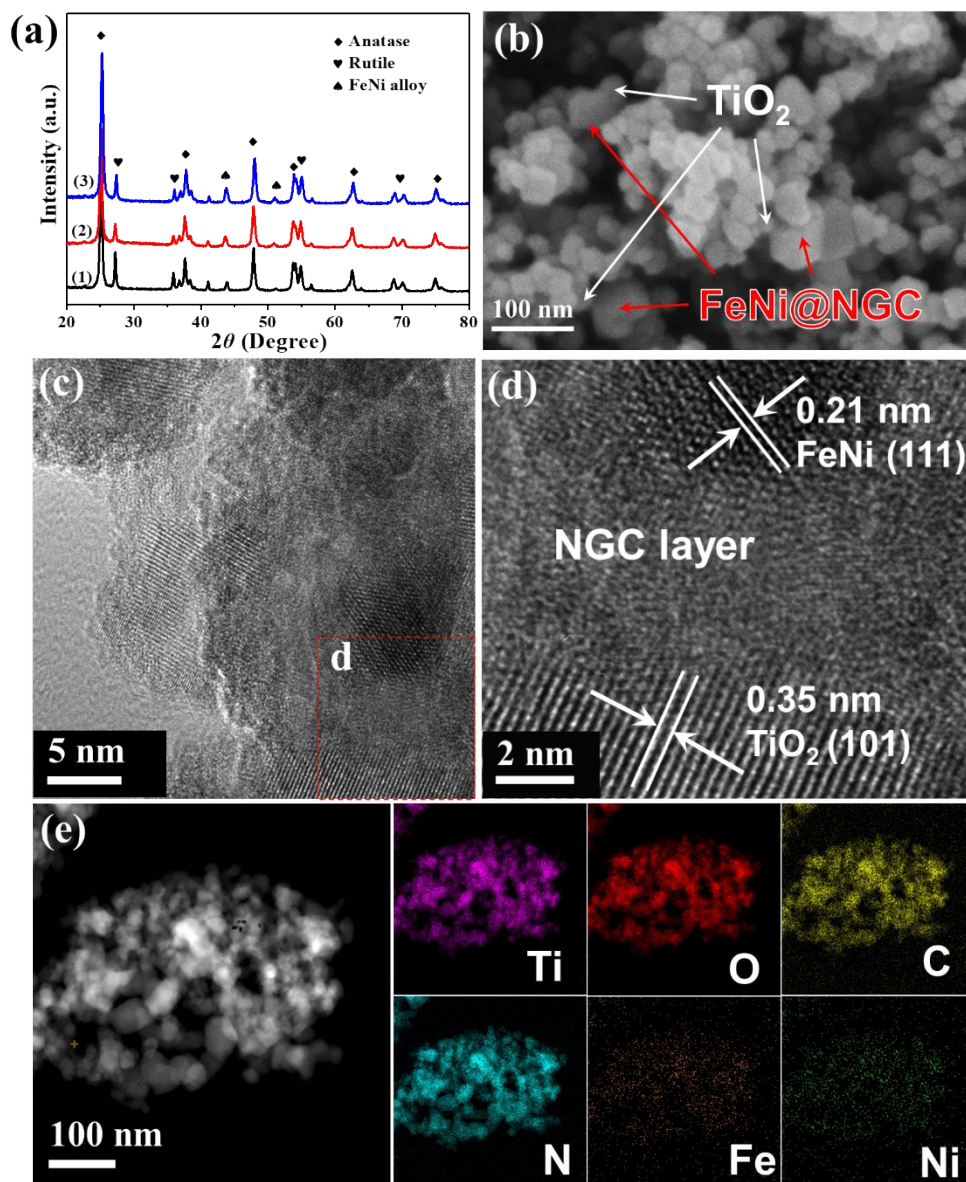
Figure S6. (a) XRD pattern of 2%-FN-TiO$_2$ (1), 4%-FN-TiO$_2$ (2) and 6%-FN-TiO$_2$ (3). (b)

SEM image of 4%-FN-TiO$_2$ sample. TEM (c) and HRTEM (d) images and corresponding

EDX elements analysis (e) of 4%-FN-TiO$_2$.
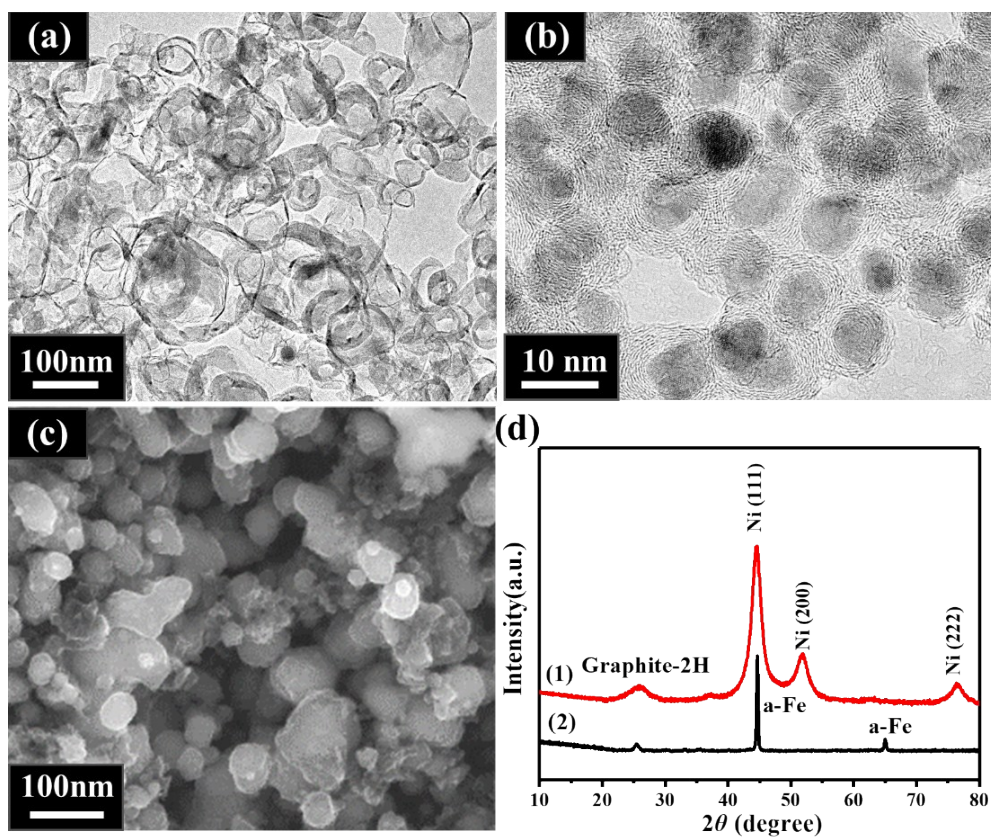
Figure S7. TEM images of HCS (a) and Ni@NGC (b); (c) SEM image of Fe@NGC; (d) XRD spectra of Ni@NGC (1) and Fe@NGC (2).

(a) 111 lattice plane (FeNi alloy)

(b) Hollow site of 3 (FeNi alloy)

(c) 110 lattice plane (Fe)

(d) 111 lattice plane (Ni)
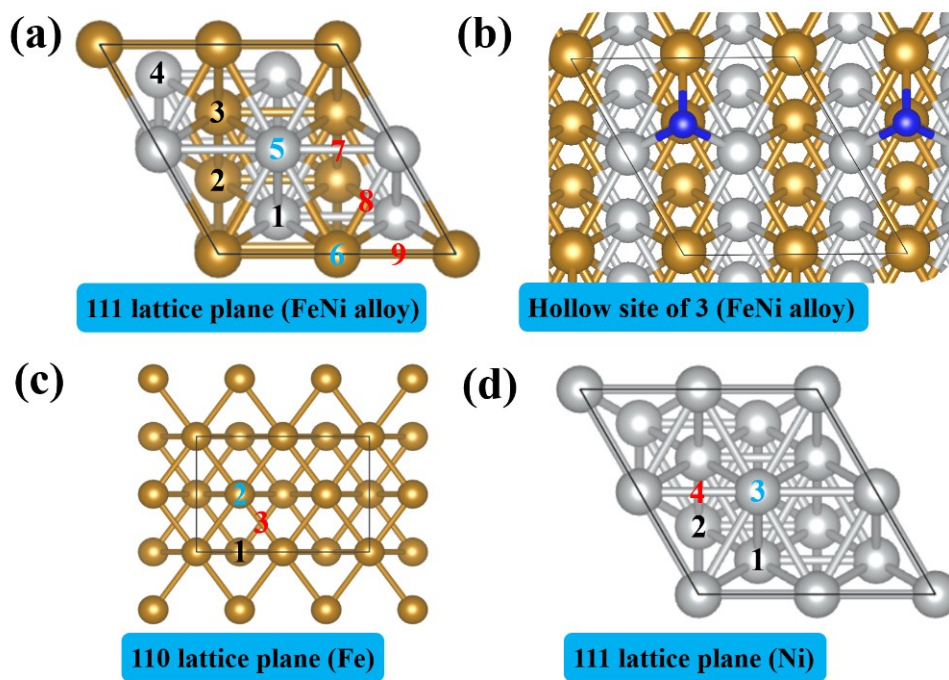
Figure S8. The (111) surface model of FeNi (a), H adsorption on the FeNi (111) surface (b), the 110 surface model of Fe (c), and the 111 surface model of Ni (d).

Figure S9. The vacuum level of Ni, Ni@NGC, FeNi and FeNi@NGC

Figure S10. CV cures of 1.0%Pt/g-C₃N₄ (a) and FNC15 (b) samples under various scan rates from 10 to 50 mV s⁻¹ in the non-Faradaic potential range (-0.4 ~ 0.3 eV vs. RHE); The corresponding C_{dl} plot of 1.0%Pt/g-C₃N₄ (c) and FNC15 (d) samples derived from current densities at -0.35 V vs RHE (in a and b) against the scan rates.
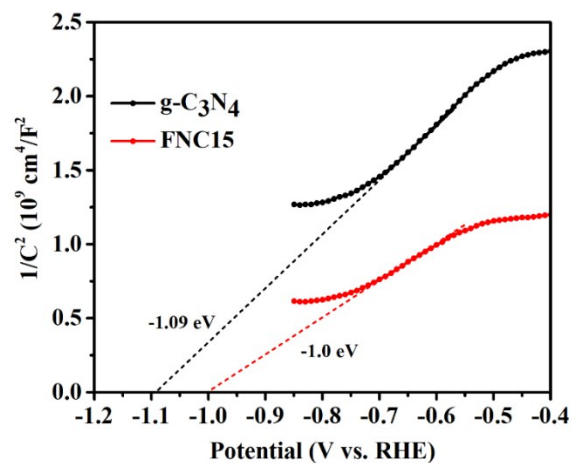
Figure S11. Mott–Schottky curves of g-C$_3$N$_4$ and FNC15 composite photocatalyst.

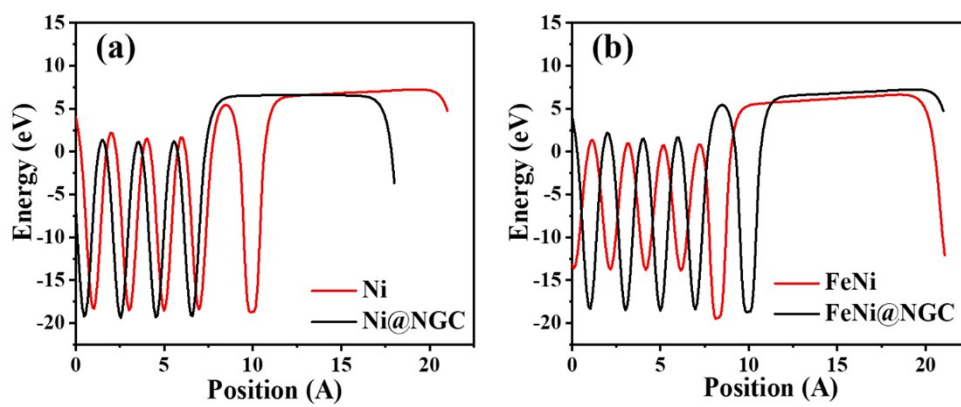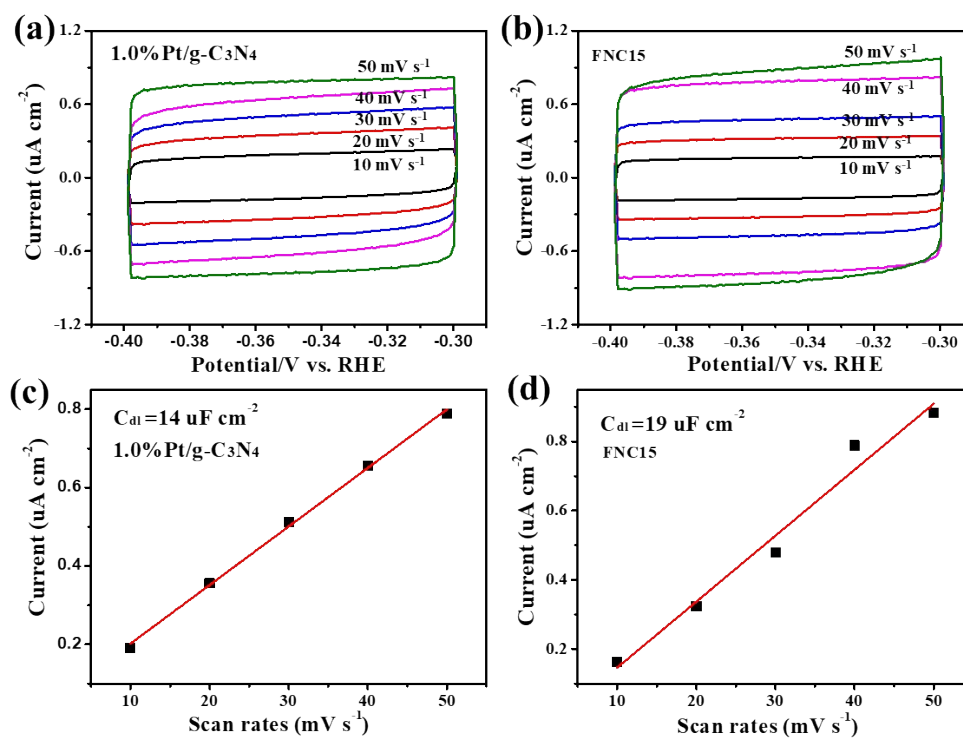As shown in Figure S10, the positive tangent slopes of linear C^{-2}/E indicate that both the g-C$_3$N$_4$ and FNC15 photocatalysts belong to n-type semiconductors.[10] The calculated flat-band potentials (V$_{fb}$) for g-C$_3$N$_4$ and FNC15 are −1.09 and -1.0 V (vs. RHE), respectively. It is known that the bottom of conduction bands (CB) is negative by −0.2 V than V$_{fb}$ for many n-type semiconductors.[11, 12] Thereby, conduction band (CB) potentials of g-C$_3$N$_4$ and FNC15 are −1.29 and −1.20 eV (vs. RHE), respectively. From the V$_{fb}$ and the bandgaps calculated from the Tauc's plots (Figure 6b), valence band (VB) potentials of g-C$_3$N$_4$ and FNC15 are 1.41, and 1.50 eV (vs. RHE), respectively.
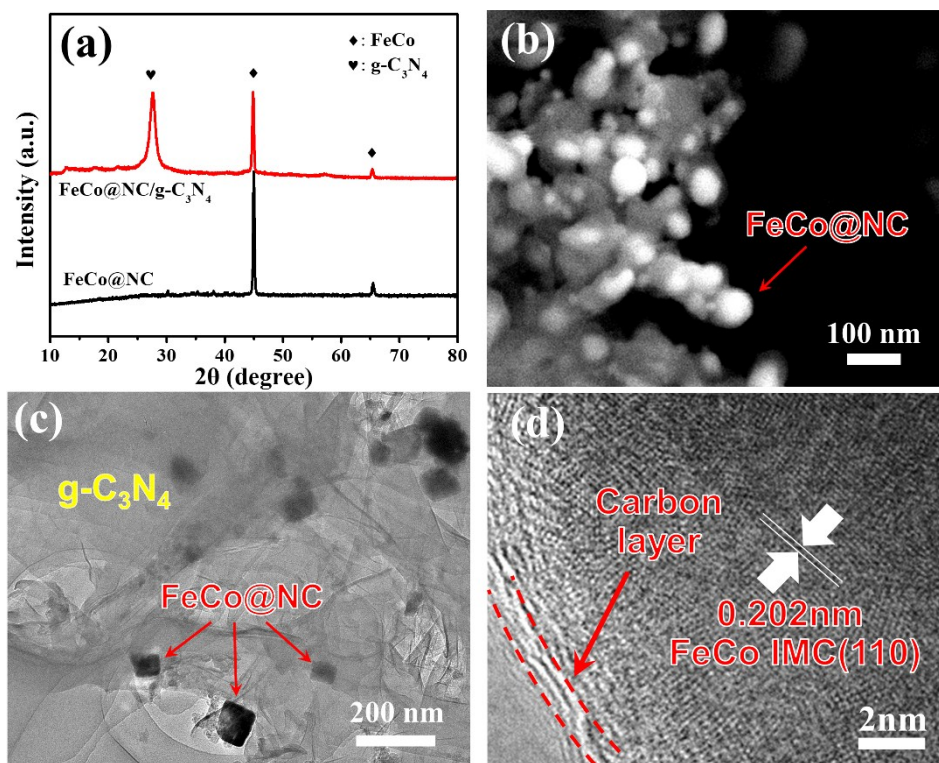
Figure S12. XRD patterns of g-C$_3$N$_4$ and FeCo@NC/g-C$_3$N$_4$ samples (a), SEM image of FeCo@NC (b), TEM image of FeCo@NC/g-C$_3$N$_4$ (c), HRTEM image of FeCo@C in FeCo@NC/g-C$_3$N$_4$ (d).

Figure S11a displays XRD diffraction peaks of FeCo@NC and FeCo@NC/g-C$_3$N$_4$. The main diffraction peak at 45° is reflected by the most exposed surface of (110) plane of FeCo alloy. The secondary peak at 65.5° is reflected by the (200) crystal plane (PDF#49-1567). XRD patterns for the FeCo@NC/g-C$_3$N$_4$ composite photocatalysts match well with that of FeCo IMC and g-C$_3$N$_4$. As shown in Figure S10b, the diameter of the FeCo@NC nanoparticles is within 50 nm and a carbon coating can be observed on the surface of the nanoparticles. The uniform distribution of FeCo@NC nanoparticles in g-C$_3$N$_4$ nanoparticles can be observed in Figure S10c. According to the lattice stripes of FeCo alloy in the HRTEM diagram of Figure S10d, the lattice width of 0.2 nm is

considered to be caused by the (110) surface of FeCo. Figure S10d also reveals the carbon layer on the surface of the FeCo@NC nanoparticles is tightly bound to g-C_3N_4. These results indicate that the FeCo@NC/g-C_3N_4 nano-heterojunction has been successfully prepared.
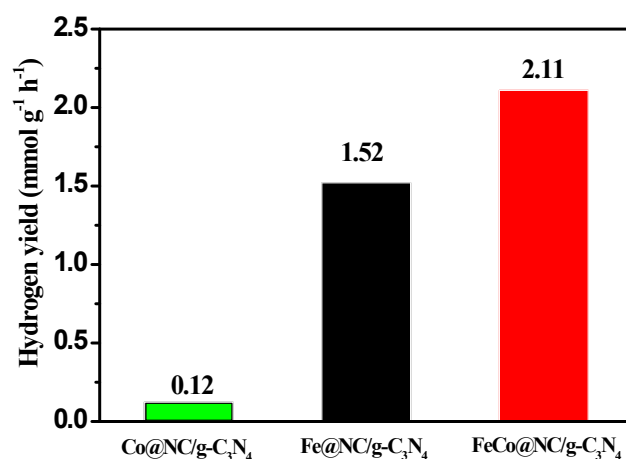
Figure S13. PC H_2 evolution rates of g-C_3N_4 loaded with Co@NC, Fe@NC and FeCo@NC under visible light irradiation.

Figure S12 shows the best FeCo@NC/g-C_3N_4 sample showed high PC efficiency of 2.11 mmol g^{-1} h^{-1} for H_2 evolution rate, which was about 222 times higher than that of g-C_3N_4. The results show that FeCo@NC nanoparticles can also be used as cocatalysts to solve the high electron-hole recombination rate of g-C_3N_4. Moreover, in order to further reflect the superior performance of the FeCo IMC, the best Fe@NC/g-C_3N_4 and Co@NC/g-C_3N_4 samples were used as the contrast group, and the PC activity was compared under the same experimental environment. The average H_2 evolution rates of Co@NC/g-C_3N_4 and Fe@NC/g-C_3N_4 were 1.52 mmol g^{-1} h^{-1} and 0.12 mmol g^{-1} h^{-1}, respectively, which were lower than those of FeCo@NC/g-C_3N_4.

Table S1. Pore structure parameters of the FeNi@NGC, FNC15 and g-C$_3$N$_4$ samples.

Samples	Specific surface area (m^2/g)	Pore size (nm)	Cumulative pore volume (cm^3/g)
g-C$_3$N$_4$	71.7381	40.5741	0.7815
FNC15	46.451	4.367	0.116
FeNi@NGC	19.303	3.468	0.079

Table S2. Summary of the PC H_2 evolution on g-C_3N_4/non noble-metal photocatalysts.

Photocatalysts	Cocatalysts, Mass ratio	Power (Xe lamp), wavelength	Activity ($\mu mol \cdot h^{-1}$), catalyst dosage	AQY	Reference (year)
g-C_3N_4	FeNi@NGC, 15 wt%	300W, $\lambda \geq 400$ nm	53.92[a], 3.31[b], 20 mg	24.49%[a] at 400 nm, 7.56%[a] at 420 nm	this work
g-C_3N_4	Ni(OH)$_2$, 1.0 mol%	350W, $\lambda > 400$ nm	8.2[a], 50 mg	1.1%[a] at 420 nm	[13] (2013)
g-C_3N_4	NiS, 1.1 wt%	300W, $\lambda \geq 420$ nm	48.2[a], 100 mg	1.9%[a] at 440 nm	[14] (2013)
g-C_3N_4	Ni/NiO, 2 wt%	300W, $\lambda \geq 420$ nm	10.0[a], 50 mg	/	[15] (2015)
g-C_3N_4	CoP, 1 wt%	300W, $\lambda \geq 420$ nm	96.20[a], 50 mg	12.4%[a] at 420 nm	[16] (2016)
g-C_3N_4	Ni@C, 2 wt%	300W, $\lambda > 420$ nm	64.5[a], 30 mg	/	[17] (2017)
g-C_3N_4	CoP, 0.25 wt%	300W, $\lambda > 420$ nm	47.44[a], 100 mg	/	[18] (2017)
g-C_3N_4	NiCoP, 2 wt%	300W, $\lambda > 420$ nm	82.15[a], 50 mg	9.4%[a] at 420 nm	[19] (2017)
g-C_3N_4	Ni$_{12}$P$_5$, 2 wt%	350W, $\lambda > 420$ nm	6.33[a], 50 mg	/	[20] (2017)
g-C_3N_4	Ni$_2$P, 1 wt%	300W, $\lambda \geq 420$ nm	14.50[a], 40 mg	1.8%[a] at 420 nm	[21] (2017)
g-C_3N_4	Co, 2.63 wt%	300W, AM 1.5G filter	11.48[a], 20 mg	6.2%[a] at 400 nm	[22] (2018)
g-C_3N_4	MoN, 50 wt%	300W, $\lambda > 420$ nm	0.89[a], 5 mg	/	[12] (2018)
g-C_3N_4	Co$_2$P, 2 wt%	300W, $\lambda > 420$ nm	27.81[a], 50 mg	/	[23] (2018)
g-C_3N_4	Co-NG, 0.05 wt%/Pt, 3.0 wt%	300W, $\lambda > 420$ nm	160.72[a], 80 mg	12.75%[a] at 420 nm	[24] (2018)
g-C_3N_4	CoS$_x$, 2 wt%	350W, $\lambda \geq 400$ nm	31.45[a], 50 mg	/	[25] (2018)
g-C_3N_4	Co$_{1.4}$Ni$_{0.6}$P, /	350W, $\lambda > 420$ nm	20.15[a], 50 mg	/	[26] (2019)
g-C_3N_4	MoS$_2$, 0.75 wt%	300W, $\lambda > 400$ nm	57.75[a], 50 mg	6.8%[a] at 420 nm	[27] (2019)
g-C_3N_4	Co@NCNT, /	300W, 148.2 mW cm^{-2}	24.16[a], 0.462[b], 20 mg	0.09%[a] at 420 nm	[28] (2019)
g-C_3N_4	CeO$_2$@MoS$_2$, /	UV-LEDs, 3W, $\lambda >$ 420 nm	65.4[a], 50 mg	10.35%[a] at 420 nm	[29] (2019)

g-C$_3$N$_4$	CoO$_x$, 7 wt%	300W, λ ≥ 420 nm	10.51[a], 40 mg	/	[30] (2019)
g-C$_3$N$_4$	Ag-Cu, 3 wt%	300W, λ ≥ 420 nm	9.84[a], 40 mg	/	[31] (2018)
g-C$_3$N$_4$	Ni, 5 wt%	300W, λ ≥ 420 nm	404.6[a], 200 mg	2.51%[a] at 420 nm	[32] (2018)
g-C$_3$N$_4$	Ni-Mo, 10 wt%	300W, λ ≥ 420 nm	35.7[a], 20 mg	0.05%[a] at 400 nm	[33] (2019)
g-C$_3$N$_4$	Fe, 0.4 atomic%	300W, λ ≥ 420 nm	0.007[methanol solution], 400 mg	/	[34] (2018)
g-C$_3$N$_4$	FeCu, 10 wt%	300W, λ ≥ 400 nm	14.44[a], 20 mg	0.974%[a] at 400 nm	[35] (2019)
g-C$_3$N$_4$	2 wt % CuS	350 W, λ > 420 nm	348 [a], 50 mg	/	[36](2019)
g-C$_3$N$_4$	15 wt % Ni$_3$C	350 W, λ > 420 nm	303.6 [a], 50 mg	0.40% at 420 nm	[37](2018)
g-C$_3$N$_4$	1 wt % Co$_2$P	350 W, λ > 420 nm	556.2[a], 50 mg	/	[38](2018)

[a] Sacrificial agent is TEOA, [b] Pure water.

Table S3. Calculation information of AQY.

Wavelength (nm)	Light intensity (mW cm^{-2})	Hydrogen evolution rate (mol s^{-1})	AQY%
400	9.3	$2.20*10^{-8}$	24.78
420	12.8	$8.83*10^{-9}$	7.28
440	21.6	$3.52*10^{-9}$	1.72
460	78	0	0

Table S4. H adsorption of Ni@NGC and FeNi@NGC in different top positions.

Sample	N-1	C-1	C-2	C-3	C-4	C-5	C-6	C-7
FeNi@NGC	0.55	0.39	0.39	0.21	-0.24	-0.35	-0.27	-0.35
Ni@NGC	0.74	-0.17	-0.17	0.23	-0.17	-0.2	-0.2	-0.2

Table S5. H Adsorption of Fe, Ni and FeNi in different positions.

Sample	1	2	3	4	5	6	7	8	9
FeNi	-0.45	-0.59	-0.54	0.34	→1	-0.54	→2	→1	→4
Fe	-1.33	-0.6	1.93	/	/	/	/	/	/
Ni	-0.53	-0.54	0.06	→2	/	/	/	/	/

Table S6. Work function, vacuum level and E-fermi of Ni, FeNi, Ni@NGC and FeNi@NGC.

Sample	Vacuum level	E-Fermi	Work function
Ni	6.55	1.49	5.06
FeNi alloy	5.78	0.87	4.91
Ni@NGC	7.43	2.54	4.89
FeNi@NGC	6.75	1.84	4.91

Table S7. Fluorescence lifetime and percentage of g-C$_3$N$_4$ and FNC15.

Sample	τ1(ns)	Rel 1%	τ2(ns)	Rel 2%	τ3(ns)	Rel 3%	τ(ns)
g-C$_3$N$_4$	80.26795	9.29488	424.3782	2.72204	10.3787	32.17306	9.31572
FeC15	60.20196	9.65174	70.08444	2.12714	383.2506	2.12664	4.956467

Part IV: References

1.   G. Kresse and J. Furthmüller, *Comp. Mater. Sci.*, 1996, **6**, 15-50.

2.   P. E. Blöchl, *Phys. Rev. B*, 1994, **50**, 17953-17979.

3.   J. P. Perdew, K. Burke and M. Ernzerhof, *Phys. Rev. Lett.*, 1996, **77**, 3865-3868.

4.   H. J. Monkhorst and J. D. Pack, *Phys. Rev. B*, 1976, **13**, 5188-5192.

5.   L. Shi, C. Ling, Y. Ouyang and J. Wang, *Nanoscale*, 2017, **9**, 533-537.

6.   H. Yin, Y.-P. Qiu, H. Dai, L.-Y. Gan, H.-B. Dai and P. Wang, *J. Phys. Chem. C*, 2018, **122**, 5443-5451.

7.   X. Zhang, P. Liu, Y. Sun, T. Zhan, Q. Liu, L. Tang, J. Guo and Y. Xia, *Inorg. Chem. Front.*, 2018, **5**, 1683-1689.

8.   G. Zhang, Z.-A. Lan, L. Lin, S. Lin and X. Wang, *Chem. Sci.*, 2016, **7**, 3062-3066.

9.   I. Tsuji, H. Kato and A. Kudo, *Angew. Chem. Int. Ed. Engl.*, 2005, **44**, 3565-3568.

10.   M. Jourshabani, Z. Shariatinia, G. Achari, C. H. Langford and A. Badiei, *J. Mater. Chem. A*, 2018, **6**, 13448-13466.

11.   A. Ishikawa, T. Takata, J. N. Kondo, M. Hara, H. Kobayashi and K. Domen, *J. Am. Chem. Soc.*, 2002, **124**, 13547-13553.

12.   S. Gong, Z. Jiang, P. Shi, J. Fan, Q. Xu and Y. Min, *Appl. Catal. B-Environ.*, 2018, **238**, 318-327.

13.   J. Yu, S. Wang, B. Cheng, Z. Lin and F. Huang, *Catal. Sci. Technol.*, 2013, **3**, 1782-1789.

14.   J. Hong, Y. Wang, Y. Wang, W. Zhang and R. Xu, *ChemSusChem*, 2013, **6**, 2263-2268.

15.   G. Zhang, G. Li and X. Wang, *ChemCatChem*, 2015, **7**, 2864-2870.

16.   C. Li, Y. Du, D. Wang, S. Yin, W. Tu, Z. Chen, M. Kraft, G. Chen and R. Xu, *Adv. Funct. Mater.*, 2017, **27**, 1604328.

17.   L. J. Fang, X. L. Wang, Y. H. Li, P. F. Liu, Y. L. Wang, H. D. Zeng and H. G. Yang, *Appl. Catal. B-Environ.*, 2017, **200**, 578-584.

18.   S.-S. Yi, J.-M. Yan, B.-R. Wulan, S.-J. Li, K.-H. Liu and Q. Jiang, *Appl. Catal. B-Environ.*, 2017, **200**, 477-483.

19.   Z. Qin, Y. Chen, Z. Huang, J. Su and L. Guo, *J. Mater. Chem. A*, 2017, **5**, 19025-19035.

20.   J. Wen, J. Xie, R. Shen, X. Li, X. Luo, H. Zhang, A. Zhang and G. Bi, *Dalton Trans.*, 2017, **46**, 1794-1802.

21.   W. Wang, T. An, G. Li, D. Xia, H. Zhao, J. C. Yu and P. K. Wong, *Appl. Catal. B-Environ.*, 2017, **217**, 570-580.

22.   N. Zhao, L. Kong, Y. Dong, G. Wang, X. Wu and P. Jiang, *ACS Appl. Mater. Interf.*, 2018, **10**, 9522-9531.

23.   R. Shen, J. Xie, H. Zhang, A. Zhang, X. Chen and X. Li, *ACS Sustain. Chem. Eng.*, 2018, **6**, 816-826.

24.   Y. Si, Y. Zhang, L. Lu, S. Zhang, Y. Chen, J. Liu, H. Jin, S. Hou, K. Dai and W. Song, *Appl. Catal. B-Environ.*, 2018, **225**, 512-518.

25.   J. Fu, C. Bie, B. Cheng, C. Jiang and J. Yu, *ACS Sustainable Chem. Eng.*, 2018, **6**, 2767-2779.

26.   R. Shen, W. Liu, D. Ren, J. Xie and X. Li, *Appl. Surf. Sci.*, 2019, **466**, 393-400.

27.   Y.-J. Yuan, Z. Shen, S. Wu, Y. Su, L. Pei, Z. Ji, M. Ding, W. Bai, Y. Chen, Z.-T. Yu and Z. Zou, *Appl. Catal. B-Environ.*, 2019, **246**, 120-128.

28.   Q. Liu, C. Zeng, Z. Xie, L. Ai, Y. Liu, Q. Zhou, J. Jiang, H. Sun and S. Wang, *Appl. Catal. B-Environ.*, 2019, **254**, 443-451.

29.   C. Zhu, Y. Wang, Z. Jiang, F. Xu, Q. Xian, C. Sun, Q. Tong, W. Zou, X. Duan and S. Wang, *Appl. Catal. B-Environ.*, 2019, **259**, 118072.

30.   Y. Zhu, T. Wan, X. Wen, D. Chu and Y. Jiang, *Appl. Catal. B-Environ.*, 2019, **244**, 814-822.

31.   Y. Zhu, A. Marianov, H. Xu, C. Lang and Y. Jiang, *ACS Appl. Mater. Interfaces*, 2018, **10**, 9468-9477.

32.   C. Sun, H. Zhang, H. Liu, X. Zheng, W. Zou, L. Dong and L. Qi, *Appl. Catal. B-Environ.*, 2018, **235**, 66-74.

33.   X. Han, D. Xu, L. An, C. Hou, Y. Li, Q. Zhang and H. Wang, *Appl. Catal. B-Environ.*, 2019, **243**, 136-144.

34.   H. Sudrajat, *Mater. Res. Express*, 2018, **5**, 095501.

35.   S. Chen, M. Li, S. Yang, X. Li and S. Zhang, *Appl. Surf. Sci.*, 2019, **492**, 571-578.

36.   R. Shen, J. Xie, P. Guo, L. Chen, X. Chen and X. Li, *ACS Appl. Energy Mater.*, 2018, **1**, 2232-2241.

37.   K. He, J. Xie, Z.Q. Liu, N. Li, X. Chen, J. Hu and X. Li, *J. Mater. Chem. A*, 2018, **6**, 13110-13122.

38.   R. Shen, J. Xie, H. Zhang, A. Zhang, X. Chen and X. Li, *ACS Sustain. Chem. Eng.*, 2017, **6**, 816-826.